VOL. 18, NO. 13, JULY 2023 ISSN 1819-6608
ARPN Journal of Engineering and Applied Sciences

www.arpnjournals.com

A REVIEW OF PEROVSKITE SOLAR CELL (PSC): ITS REVOLUTION AND MATHEMATICAL MODELLING

Lee Jin Yao[1], Rahifa Binti Ranom[1], Kyairul Azmi Baharin[1] and Norhafizah Md Sarif[2]
[1]Fakulti Kejuruteraan Elektrik (FKE), Universiti Teknikal Malaysia Melaka (UTeM), Hang Tuah Jaya, Durian Tunggal, Melaka, Malaysia
[2]Centre for Mathematical Sciences, Universiti Malaysia Pahang Al-Sultan Abdullah, 26300 Gambang, Pahang
E-Mail: m012120006@student.utem.edu.my

ABSTRACT

Perovskite solar cell (PSC) is one of the third-generation type of solar cells that has high efficiency and can be produced at a lower cost compared to silicon-based solar cells. However, one of its core problems is the uncertainty of its short- and long-term stability. To minimise this risk, proper modelling is required to assess its potential performance before fabrication. Modelling of PSC is also important to prevent wastage of time and optimise material use. This work provides a comprehensive review of current PSC circuitry and the electrochemical modelling techniques available. Circuitry modelling relates to the operation conditions where PSC is represented by an equivalent circuit model that contains a resistor, diode, photo-generated current source, and others. Meanwhile, electrochemical modelling refers to the operation mechanism of PSC and can be represented by mathematical equations that include parameters of charge density of the layers, drift, diffusion, generation, and recombination process of charge carriers. This paper also summarizes the numerical algorithms and modelling simulations used such as SCAPS, AFORS-HET, COMSOL Multiphysics, MATLAB to evaluate PSC model performance. Through this paper, a summary of the modelling results has been compiled covering various aspects of fabrication including the material's layer thickness, doping concentration, electron affinities as well as temperature distribution within the PSC during operation.

Keywords: perovskite solar cells, circuitry modelling, electrochemical modelling, steady-state, numerical simulation.

Manuscript Received 22 February 2023; Revised 24 August 2023; Published 13 September 2023

INTRODUCTION

Solar is a form of sustainable energy that can convert sunlight into electricity [1]. Table-1 depicts the process of developing power conversion tech that transforms solar power into electricity:

Table-1. The process of developing power conversion tech that transforms solar power into electricity.

Year	Process
1839	Alexandre Edmond Becquerel, a French physicist, discovered the photovoltaic effect by immersing a cell composed of metal anode and cathode in an electrolyte liquid and exposing it to light [2].
1877	William Grylls Adams and Richard Evans Day applied the photovoltaic principle that was discovered by Alexandre Edmond Becquerel in selenium [2].
1883	Charles Fritz invented the first selenium solar cell [2].
1940	Russell Shoemaker Ohl found that current flowed through silicon samples which had cracked in the middle when the sample was exposed to light [3].
1946	Russell Shoemaker Ohl patented the silicon solar cell with around 1% efficiency [4].
1954	Bell Labs scientists developed the very first practical solar cell using silicon with a 6% effectiveness [2].

THE REVOLUTION OF SOLAR CELL

The solar cell underwent a few revolutions over several decades from the first generation of silicon solar cells developed in 1954 until now. Table-2 compares the three generations of solar cells [5]. Among the third-generation solar cells, the efficiency of power conversion for perovskite solar cells (PSC) has growth with swiftly within a short time interval compared to other materials as it has tremendous potential in the future to upgrade solar cell performance to the next level in terms of increased power conversion efficiency and stability but with lower manufacturing costs. In this paper, the PSC will be explained in terms of their materials, structure architecture, and operation principles. The modelling of PSC conducted by researchers with different approaches will be reviewed in this paper to have a better understanding of the process of converting solar energy to electrical energy in PSC and extract the parameters that are involved in the related processes.

PEROVSKITE CRYSTAL STRUCTURE, MATERIALS, AND SOLAR CELL ARCHITECTURE

Perovskite is a natural mineral material found in the Ural Mountains in Russia. The founder of the perovskite is a mineralogist named L. A. Perovski who found the perovskite in 1839 composed of calcium, titanium, and oxygen with the chemical formula $CaTiO_3$ [6]. After that, an organic-inorganic lead or tin halide compound that has a similar material with the formula ABX_3 was considered a perovskite compound. In ABX_3

perovskite compound, A represents a large organic monovalent cation (Ca^+, $CH_3NH_3^+$, $C_2H_5NH_3^+$, $C_3N_3H_6^+$, $NH_2CH{=}NH_2^+$, etc.) which constitutes the cuboctahedra sites in a cubic space, B represents a small divalent metal cation (Pb_2^+, Sn_2^+, Bi_2^+, Ge_2^+, etc) which constitute the octahedral sites in a cubic space, and X represents a halide anion (F^-, Cl^-, Br^-, I^-, etc). Figure-1 shows the compound structure of perovskite [6].

Table-2. The three generations and types of solar cells [5].

First Generation: Wafer Based	Second Generation: Thin Films Based	Third Generation
1. Monocrystalline silicon • made of single-crystal silicon with perfect lattice arrangement, higher material purity, and weak internal resistance [7]. • higher efficiency than polycrystalline silicon solar cells [8]. • higher cost than the polycrystalline silicon solar cell due to the costly manufacturing process [9]. • 27.6% efficiency in January 2022 [10]. 2. Polycrystalline silicon • made out of recrystallized silicon with nonuniform lattices [8]. • 23.3% efficiency in January 2022 [10].	1. Cadmium Telluride (CdTe) • developed by Bonnet and Rabnehorst which reported 6% efficiency in 1972. • 22.1% efficiency in January 2022 [10]. 2. Amorphous thin-film silicon (α-Si: H) • fabricated by Carlson and Wronski at RCA Laboratory which reported 2.4% efficiency in 1976 [11]. • 14.0% efficiency in January 2022 [10]. 3. Copper Indium Gallium Selenide (CIGS) • created by Kazmerski which reported 4.5% efficiency in 1976 [11]. • 23.4% efficiency in January 2022 [10].	1. Dye-sensitized solar cells (DSSC) • consists of dye sensitizers as a light absorber. • invented by Brian O'Regan and Michael Grätzel at UC Berkeley with 7% efficiency [12]. • 13.0% efficiency in January 2022 [10]. 2. Quantum dots solar cells (QDSC) • introduced by Burnham and Duggan in 1990 to replace dye. • recorded 9% efficiency in 1990 [13]. • 18.1% efficiency in January 2022 [10]. 3. Perovskite solar cells (PSC) • invented by Tsutomu Miyasaka in 2009. • using an organic-inorganic lead halide perovskite compound as light absorbers. • efficiency was just 3.8% in 2009 [14]. • 25.5% efficiency in January 2022 [10].
Advantage: stable and high efficiency. Drawback: high manufacturing cost [7].	Advantage: lower manufacturing costs [7]. Drawback: lower efficiency, toxicity, and the rarity of materials such as cadmium will cause illness for humans and animals as well as create a lot of environmental issues [15].	Advantage: easier fabrication, low cost of manufacturing, high efficiency, and cost-effectiveness. Drawback: fast degradation after overexposure to heat, moisture, snow, etc, presence of toxins such as lead in perovskite layer.

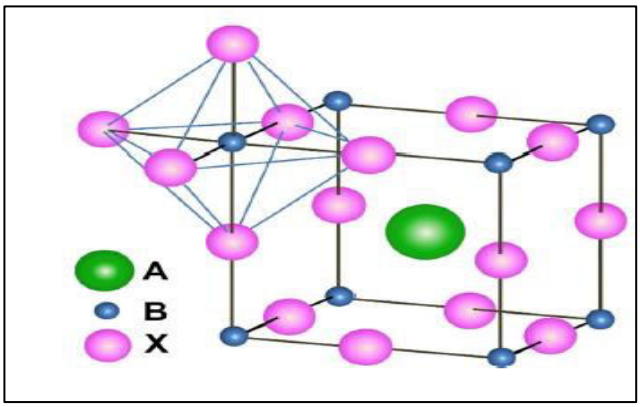

Figure-1. The compound structure of perovskite showing BX6 octahedral and larger A cation occupied in cuboctahedra site [6].

Besides the materials and crystal structure of perovskite, the normal and inverted structures of planar and mesoscopic PSC are discussed in this part. The structure layer of PSC can be categorized as normal structure (n-i-p) and inverted structure (p-i-n), where n refers to the negatively doped layer, i refers to the intrinsic layer, and p refers to the positively doped layer [16]. In PSC, the negatively doped layer and positively doped layer are made up of electron transporting material (ETM) and hole transporting material (HTM) respectively, while the intrinsic layer is made up of perovskite material. However, the materials of ETM and HTM are dependent on the PSC manufactured in a normal structure or inverted structure. This is due to the fact that the transport materials placed on the outer boundary of the cell that is initially received by the sun's radiation are different [6]. The cathode and anode for both structures of PSC are different, in which the electrodes for n-i-p structure use transparent conductive oxide (TCO) and conductive metal respectively, while for the p-i-n the structure is vice versa. Besides this, both structures can be divided into mesoscopic and planar structures. The mesoscopic structure consists of a mesoporous layer, while all the layers of planar structures are presented in planar [6]. Figure-2 shows the PSC in four different structures [17].

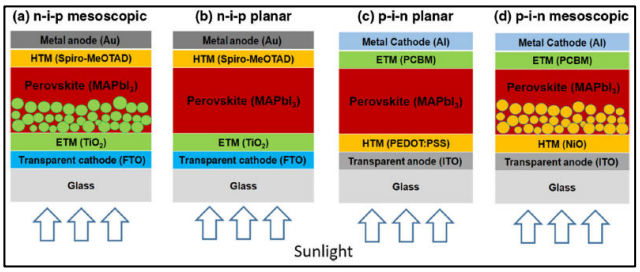

Figure-2. The perovskite solar cell in four different structures [17].

The architecture of perovskite solar cells (PSC) in mesoscopic structure was developed by modifying the solid-state dye-sensitized solar cells (DSSCs) architecture by replacing the light-harvesting dye with lead halide perovskite semiconductors [6] [17] [18]. Thus, the operation of PSC is similar to that of DSSCs and organic photovoltaic aid [6]. The first PSC in n-i-p mesoscopic structure was fabricated by Kojima in 2009 by using mesoporous TiO_2 film, iodide/triiodide redox couple liquid electrolyte, and platinum counter electrode [13][16]. The regarding PSC that uses perovskite materials $CH_3NH_3PbBr_3$ and $CH_3NH_3PbI_3$ as sensitizers recorded efficiencies of 3.13% and 3.81% [13].

The mesoscopic metal oxide layer serves as a scaffold for perovskite material to adsorb the perovskite and allows the perovskite absorber to adhere to the mesoscopic metal oxide framework [16][19]. Besides this, the mesoscopic metal oxide layer can also increase the light-receiving area of the photosensitive material and improve the efficiency of PSC by promoting electron transport between the perovskite absorber and the FTO electrode [18][19]. Although completely filling the pores of a mesoporous structure can increase the photon absorption, enhance carriers' collection, and prevent direct current leakage between the two contacts, a thicker mesoporous structure reduces PSC performance by lowering its open circuit voltage and short circuit current because there is not enough area for adequate grain growth in the perovskite materials confined within the pores [18]. By carefully regulating the interfaces between the various PSC layers, it is also possible to obtain high efficiency without the mesoporous layer [6].

The planar structure of PSC is considered an improvement from the mesoscopic structure because it can achieve similar efficiency with a thinner, simplified composition [17][18]. In addition, the planar structure of PSC requires lower temperatures in the fabricating process compared to the mesoscopic structure [6]. The n-i-p planar structure of PSC which was fabricated by Zhou et al in 2014 was reported at 19.3% efficiency, while the p-i-n (inverted) planar structure of PSC fabricated by Dong *et al* in 2015 was reported at 18.9% efficiency [17]. However, the efficiency for the mesoscopic structure of PSC was still higher than the planar structure of PSC, as the mesoscopic TiO_2/$FAPbI_3$ perovskite solar cell reported by Yang et al. at the end of 2014 had achieved an efficiency greater than 20% [19]. Due to this, many high-efficiency solar cells implement the mesoscopic structures with n-i-p configuration [17].

PEROVSKITE SOLAR CELLS OPERATION PRINCIPLE

In this part, the way perovskite solar cells (PSC) convert solar energy to electrical energy is discussed. The perovskite in the PSC functions as a light absorber. When the incident light falls on PSC, the generation of electrons and holes occurs. The perovskite absorbs the photon from the light and the electrons in the perovskite will undergo excitation after receiving enough photon energy and leave the holes [6]. After the electrons excite to the conduction bands or the lowest unoccupied molecular orbital (LUMO) and leave the holes at the valence bands or the highest occupied molecular orbital (HOMO), the electrons are injected into the electron transporting layer (ETL) and migrate to the cathode, while the holes are injected to the hole transporting layer (HTL) and migrate to the anode [20]. To ensure the electrons would not transfer to HTL and the holes would not transfer to the ETL, the conduction band of the HTL material that is selected must be higher than the perovskite conduction band while the valence band of the ETL material that is selected must be lower than the perovskite valence band [21]. The electrons at the cathode will flow to the anode via the external circuit and mix with the holes to complete the recombination process, the drift current is generated in the circuit and flows in the opposite direction. When electrons recombine with holes, they will cancel each other and become neutral, which stops their involvement in the electric current. Figure-3 shows the structure of the HOMO/valence bands (dashed lines) and LUMO/conduction bands (solid lines) of PSC and the flow of electrons and holes [20].

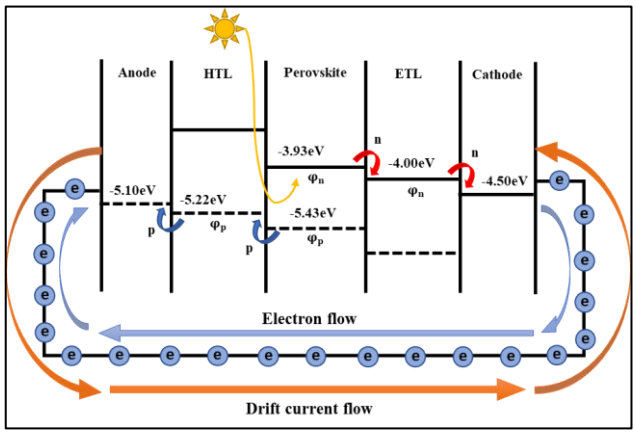

Figure-3. The structure of the HOMO/valence bands (dashed lines) and LUMO/conduction bands (solid lines) of PSC and the flow of electrons and holes [20].

If compared with the schematic of a simple silicon solar cell, the perovskite layer in PSC is similar to the p-n junction in a simple silicon solar cell with the function of absorbing photons from different wavelengths to begin the generation process to generate electrons and

holes and migrate to ETL and HTL respectively [20]. Besides that, the ETL and HTL in PSC are also similar to the negatively doped and positively doped layers in simple silicon solar cells. The perovskite material in PSC can absorb more photons from a wide range of wavelengths with a high light absorption coefficient, this advantage enables perovskite to generate more electron-hole pairs since with more electrons, it is easier to gain enough photon energy and excite the conduction band and leave the holes at the valence band.

According to Pratik Mandon and Eswara Prasad, the value of the global PSC market size recorded in 2020 might be forecast to increase from 0.4 billion US dollars to 6.6 billion by 2030 [22]. The demand for PSC is increasing all over the world due to its high power conversion efficiency (PCE) due to the absorber material used. Perovskite materials have excellent light absorption that can react with various wavelengths of light to convert more sunlight into electricity. The cheaper cost of PSC is always a concern for manufacturers, investors, and installers. According to Nanyang Technological University (NTU) scientists, the prices for the next generation of solar cells made of organic-inorganic hybrid perovskite materials are five times cheaper than previous thin-film solar cells and can be manufactured by using a simple solution-based manufacturing process [23]. Besides that, the flexibility and lightweight features of PSC are also attractive points for various end-users such as the aerospace, industrial automation, electronics, and energy consumer fields. However, there are some drawbacks or disadvantages of PSC that still need to be studied to enhance their quality and reduce the negative impact on the environment. For example, PSC undergoes fast degradation due to the perovskite breaking down quickly after overexposure to heat, moisture, snow, etc. The presence of toxins such as lead contained in methylammonium lead halide perovskite ($CH_3NH_3PbX_3$) materials is harmful to the environment and a serious health hazard. Apart from that, the thickness of the perovskite layer is also a main issue that affects the PCE of PSC [24]. Therefore, R&D efforts as well as technical developments regarding PSC are continuously improved to enhance the PSC in different aspects such as stability, PCE, and replacing the toxic material with non-toxic substitutes.

MODELLING OF PSC

In this paper, the circuitry and electrochemical modelling of PSC will be reviewed. Circuitry modelling can derive the expressions of bulk and surface recombination currents analytically as well as describe the current density-voltage characteristics of practical PSC with an equivalent circuit model. Since the optical loss, series, and shunt resistance losses, as well as bulk and surface recombination losses, are taken into consideration in the equivalent circuit model, the efficiency loss ratios under the open-circuit voltage condition can be calculated and the loss mechanisms can be more understood [25]. On the other hand, electrochemical modelling can explain the behaviour of PSC with the motion of ion vacancies and electronic charge carriers. When free charges migrate through the perovskite via thermally excited diffusion and electrically induced drift, electrical properties for PSC such as total current density and drift voltage of charge carriers can be calculated. Apart from that, the Poisson equation in electrochemical modelling that involves the ionized doping concentration for the acceptor and donor is used to calculate the electrostatic potential of PSC [20].

Circuitry Modelling

Circuitry modelling of PSC is representing its structure into an equivalent circuit model (ECM) to investigate the performance of PSC through simulation. This model includes some electronic components that refer to the related operation conditions of PSC. The level of detail for the ECM model is dependent on the number of parameters to be included. The more detailed the model, the more parameters such as impedance, diode ideal factors, and saturation currents are required for modelling. The difficulty in obtaining these parameters also increases depending on the complexity of the equivalent circuit model. Single-diode, double-diode, and triple-diode models are three common models that have been developed to describe the solar cell. The accuracy of modelling for triple-diode ECM is higher than for single-diode and double-diode ECM.

The single-diode model that connects one diode with series and parallel resistors is the basic model in circuitry modelling of solar cell. For example, Figure-4 shows the single-diode models of PSC which considers the practical aspects that arise due to fabrication conditions, which is represented in terms of resistances and an ideality factor [26]. The shunt resistance, R_{sh} represents the leakage current loss induced by the inevitable defects of PSC such as traps and pinholes, while series resistance, R_s represents the net effect of the current loss at both electrodes, HTL, ETL, and interfaces of perovskite layer [25]. The constant current source produces the photogenerated current, J_L. To measure the photo-generated current, diode saturation current, ideality factor, shunt, and series resistances, E. Velilla *et al*. simulated single-diode models of p-i-n planar PSC [27]. On the basis of the fewer errors discovered during the optimization process and a lower ideality factor of 1.4, they claim that the single-diode model is suitable for producing the I-V curve of PSC. This is due to the fact that higher ideality factors will result in lower fill factors, which will then produce lower efficiencies and higher losses, as indicated by lower shunt resistances. According to Gagandeep et al, in practice, it is difficult to obtain a very high value of shunt resistance for PSC [28].

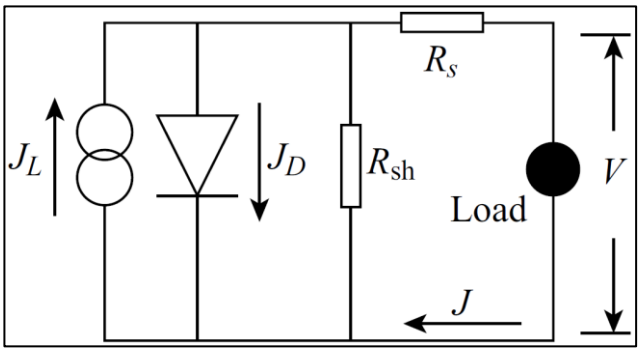

Figure-4. Single-diode equivalent circuit model of PSC [26].

The optimum single heterojunction equivalent circuit's diode ideal factor often falls between 1 and 2. The p-n junction quality which affects recombination at the ETL/perovskite and perovskite/HTL interface is reflected in this diode ideal factor. In order to simulate the I-V characteristic of p-i-n planar PSC and analyses SRH recombination current, direct recombination current, diffusion current, as well as carrier recombination and transportation characteristics, P.Liao *et al*. modified the basic equivalent circuit by adding double heterojunctions in series [26]. To resolve the problem of the diode ideal factor being bigger than 2 from a single-diode model equivalent circuit, the double PN junction model of PSC is proposed and shown in Figure-5.

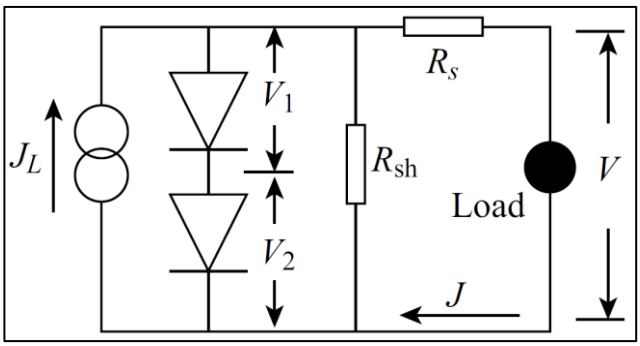

Figure-5. Double p-n junction equivalent circuit model of PSC [26].

By comparing the single-diode equivalent circuit model with a double p-n junction equivalent circuit model, there is very limited information that can be obtained by fitting the dark current into the equation that is obtained from a single-diode equivalent circuit model. The equation that is obtained from the single-diode equivalent circuit model also cannot embody the different physical processes for the dark current curve slope exponentially increasing varies with the voltage [26]. Dark current is the forward bias current of the PN junction diode under the sunlight due to the diffusion of minority carriers generated thermally within a diffusion length of the depletion region. Such charges are constantly generating and recombining due to the thermal excitation of the material, the bulk recombination current should be the dominant dark current mechanism in PSC [26][29][30].

To increase the accuracy of the conventional equivalent circuit model of PSC and provide a more accurate approximation of the device parameters, a parallel double diode equivalent circuit model is developed as show in Figure-6 [31]. Besides modelling the diffusion and recombination in the quasi-neutral regions (QNRs) of the emitter and bulk regions of the p-n junction of PSC with diode D_1, the charge carriers' recombination that takes place in the space charge region (SCR) is modelled with diode D_2. A.Bărar et al. have compared the maximum power point, fill factor, and PCE of a single-diode and a parallel double-diode equivalent circuit model that is yielded after fitted into the I-V curve with the values of dark saturation current, series, and parallel resistance that is extracted from both equivalent circuit models by using the Lambert W function [31]. Results show that the parameters used for the parallel double-diode equivalent circuit model are much closer to the values from the experimental data. This indicates that the parallel double-diode equivalent circuit model has better accuracy than the single-diode equivalent circuit model.

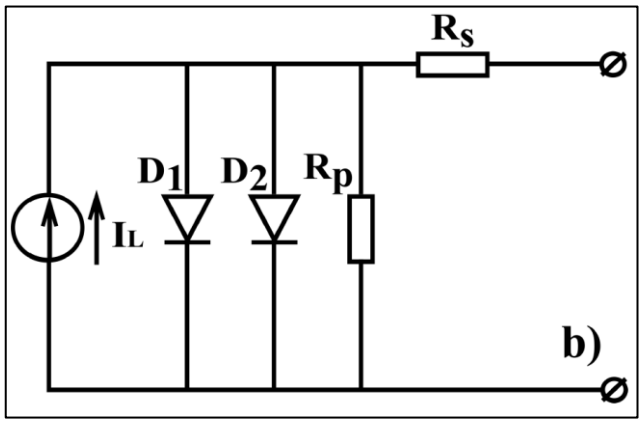

Figure-6. Parallel double diode equivalent circuit model of PSC [31].

Next, a parallel triple diode equivalent circuit model of PSC has been modelled as well, shown in Figure-7 [32]. The third diode is added in parallel to the existing parallel double-diode equivalent circuit model which models the recombination in the defect regions, grain sites, etc. D.S.Abdelminaam et.al. have conducted parameters extraction for parallel double diode and parallel triple diode equivalent circuit model by using Turbulent Flow of Water-based Optimization (TFWO) [33]. The results show that the maximum absolute error for current and power that are extracted from the parallel triple diode equivalent circuit model is lower than the parallel double diode equivalent circuit model. This indicates that the accuracy of parallel triple diode equivalent circuit model is better than parallel double diode equivalent circuit model.

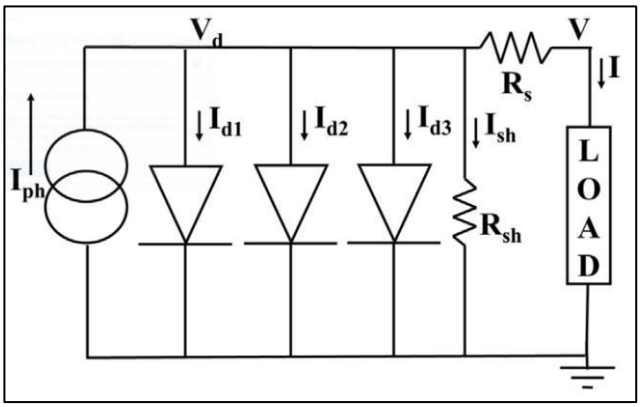

Figure-7. Parallel triple diode equivalent circuit model of PSC [32].

The Equivalent Circuit Model of PSC and its Analytical Solution

The analytical solution is well-defined in terms of known functions or constants that frame the problem in a well-understood form. The problem can be solved by using the exact solution once it has been defined.

According to a generalised equivalent circuit of a planar heterojunction perovskite solar cell (PSC), N. Santakrus and colleagues have proposed an analytical solution to the transcendental J-V equation [34]. It is able to use the Lambert W-function through circuit simplification to derive the transcendental J-V equation of the equivalent circuit, which includes the explicit analytical formulas for current and voltage. The equivalent circuit is shown in Figure-8. Based on this figure, the output current density, J can be presented by the equations below:

$$J = J_{ph} - J_{sh} - J_d \quad (1)$$

$$J = J_{ph} - \frac{V+JR_s}{R_{sh}} - J_0\left(e^{\frac{V+JR_s}{V_{th}(n_1+n_2)}} - 1\right) \quad (2)$$

where J_{ph}, J_{sh}, J_d, R_{sh}, and R_s are the photocurrent densities produced in the cell when light strikes it, the current flowing through the shunt resistor, the current through the double diode, the shunt resistance caused by the reverse saturation current of the active junction, and the internal resistance induced by ETL, HTL, and metal contacts. The ideality factors of diodes D_1 and D_2 are n_1 and n_2 respectively, V is the sum of the voltages across the two diodes connected in series, and J_0 is the reverse saturation current.

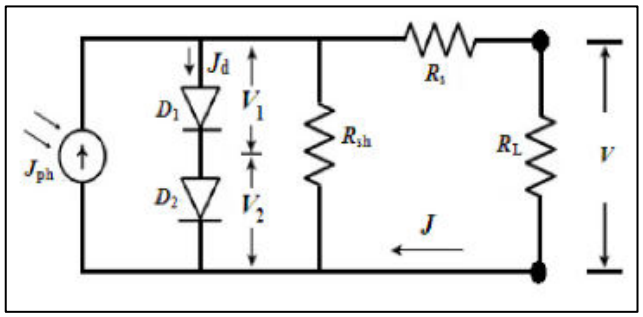

Figure-8. Equivalent circuit of a planar-structured perovskite solar cell as proposed by Liao *et al* [26].

Eqn. (2) can be solved by using the Lambert W-function in the expression of J and V as shown below:

$$V = (J_{ph} + J_0 - J)R_{sh} - JR_s - (n_1 + n_2)V_{th}L_V \quad (3)$$

$$L_V = LambertW\left[\frac{J_0R_{sh}e^{\frac{R_{sh}(J-J_{ph}-J_0)}{(n_1+n_2)V_{th}}}}{(n_1+n_2)V_{th}}\right] \quad (4)$$

$$J = -\frac{V}{R_s+R_{sh}} + \frac{R_{sh}(J_{ph}+J_0)}{R_s+R_{sh}} - \frac{(n_1+n_2)V_{th}}{R_s}L_J \quad (5)$$

$$L_J = LambertW\left[\frac{\frac{R_{sh}(R_sJ_{ph}-R_sJ_0+V)}{(n_1+n_2)V_{th}(R_s+R_{sh})}}{(n_1+n_2)V_{th}(R_s+R_{sh})}\right] \quad (6)$$

To obtain the open circuit voltage equation, the value of J in eqn. (3) and eqn. (4) are set to zero. On the other hand, the value of V in eqn. (5) and eqn. (6) are set to zero to obtain the short circuit current equation. At the same time, the model parameters (R_{sh}, R_s, J_0, J_{ph}) based on different planar PSC need to substitute into eqn. (3) to eqn. (6) to obtain the values of open circuit voltage and short circuit current respectively. The power delivered at an external load is given by $P = JV$ and can be expressed in terms of J and V as shown in the eqn. (7) and eqn. (8).

$$P(J) = J\{(J_{ph} + J_0 - J)R_{sh} - JR_s - (n_1 + n_2)V_{th}L_V\} \quad (7)$$

$$P(V) = \left\{-\frac{V}{R_s+R_{sh}} + \frac{R_{sh}(J_{ph}+J_0)}{R_s+R_{sh}} - \frac{(n_1+n_2)V_{th}}{R_s}L_J\right\}V \quad (8)$$

To determine the current and voltage at the maximum power delivered by the device, the model parameters (R_{sh}, R_s, J_0, J_{ph}) based on different planar PSC need to be substituted into eqn. (7) and eqn. (8). Next, the derivatives of these equations need to be set to the following conditions:

$$\left(\frac{\partial P(J)}{\partial J}\right)_{J=J_{mp}} = 0 \quad (9)$$

$$\left(\frac{\partial P(V)}{\partial V}\right)_{V=V_{mp}} = 0 \quad (10)$$

At the end, after obtaining the open circuit voltage, V_{oc}, short circuit current, J_{sc}, current at the maximum power, J_{mp}, and voltage at the maximum power, V_{mp}, the fill factor, FF and efficiency, η of PSC can be calculated by the equations below:

$$FF = \frac{J_{mp}V_{mp}}{J_{sc}V_{oc}} \quad (11)$$

$$\eta = \frac{P_{max}}{P_{in}} = \frac{J_{mp}V_{mp}}{P_{in}} \quad (12)$$

where P_{max} is the maximum output power and P_{in} is the input power (100 mWcm^{-2}). The planar-structured PSC performance characteristics, including short circuit current, open circuit voltage, fill factor, and efficiency, are estimated throughout these mathematical solutions and contrasted with experimentally obtained values. Because the method produces precise explicit expressions, N. Santakrus *et al*. demonstrated that using the Lambert W-function for the equivalent circuit is advantageous in the inquiry and may be utilised to explore some PSC properties in order to get closer to their ideal condition [34].

In the paper of M.Rasheed et al [35], the analytical equations of solar cell are obtained by characterizing the solar cell into the analytical model of a single-diode design. The analytical model is shown below:

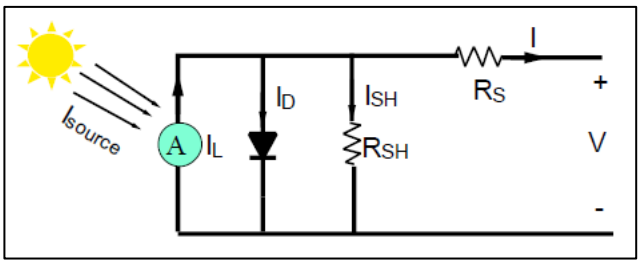

Figure-9. Single-diode electrical equivalent circuit model of a solar cell [35].

The equation of this equivalent circuit that shown in Figure-9 is given by:

$$I = I_L - I_{SH} - I_D \quad (13)$$

$$I_D = I_0\left(e^{\frac{V_D}{nV_{th}}} - 1\right) \quad (14)$$

$$I_{SH} = \frac{V+IR_s}{R_{SH}} \quad (15)$$

where I_L, I_{SH}, I_D, I_0 and I are the photocurrent density generated in the cell when light falls on it, the current flow through the shunt resistor, the dark current that flows through diode, the reverse saturation current, and the output current of PSC in respectively. While R_s, R_{SH}, V_{th}, V_D and V are the internal resistance, the shunt resistance due to the reverse saturation current of the active junction, the thermal voltage, the voltage of the diode and output voltage. Hence, $V_D = V$ in parallel and $V_{th} = \frac{k_bT}{q}$, where $k_b = 1.38 \times 10^{-23}$ J/K , $T = 298.15$ K, $q = 1.6 \times 10^{-19}$ C, therefore $V_{th} = 0.026$ V. The recombination factor closeness to an ideal diode, n is equal to 1.2 and the reverse saturation current, I_0 is equal to 10^{-12} A. By substitute eqn. (14) and eqn. (15) into eqn. (13) with the known value of parameters, the equivalent circuit equation is shown in below:

$$\frac{V}{R} = I_L - \frac{V+IR_s}{R_{SH}} - 10^{-12}\left(e^{\frac{V}{1.2(0.026)}} - 1\right) \quad (16)$$

according to M.Rasheed et al [35], V can be calculated numerically by the first derivative of eqn. (16).

Electrochemical Modelling

In electrochemical modelling, the physics of the perovskite solar cells (PSC) are typically represented by a series of partial differential equations (PDEs). It can be utilised to comprehend the charge density at the PSC layers as well as the generation, recombination, drift, and diffusion processes of charge carriers. PDEs are solved using spatial discretization techniques like finite element and finite difference. These techniques require discretizing the electrochemical model, which leads to a number of equations [36].

Drift-Diffusion Model

The electrochemical modelling of PSC can be represented by the drift-diffusion equation which describes the transport process of the ion vacancies and electronic charge carriers in PSC [21]. The drift-diffusion model is an important tool to have a better understanding about the mechanism and behavior of PSC through understanding the carrier dynamics. The drift-diffusion model consists of the Poisson, drift-diffusion and continuity equations [37].

Generally, the Poisson equation describes the relation between electrostatic potential and charge density. The electrostatic potential is related to the charge density because of the electric field [38]. The divergence relationship between the electric field and the charge density is shown in equation below:

$$\nabla . E = \frac{q}{\varepsilon} \quad (17)$$

where E is the electric field, q is the charge density, ε is the dielectric permittivity and φ is the electrostatic potential. The gradient relationship between the electric field and the electric potential is shown below [39]:

$$E = -\nabla\varphi \quad (18)$$

by substituting eqn. (18) into eqn. (17), the Poisson equation can be rewritten as:

$$\nabla.(-\nabla\varphi) = \frac{q}{\varepsilon} \quad (19)$$

$$\nabla^2\varphi = -\frac{q}{\varepsilon} \quad (20)$$

However, the Poisson equation that describes perovskite solar cell (PSC) operation is affected by the concentrations of electrons, holes, ionized donors, and ionized acceptors which are shown below:

$$\nabla^2\varphi = \frac{\partial^2\varphi}{\partial x^2} = -\frac{q}{\varepsilon}(-p(x) + n(x) - N_D^+(x) + N_A^-(x)) \quad (21)$$

where p is the number of free holes, n is the number of free electrons, N_D^+ is the donor ionized doping concentration, N_A^- is the acceptor ionized doping concentration, and x is the thickness of the solar cell [40].

Next, the drift-diffusion equations are utilized to obtain the total current density for electrons and holes which are similar with the drift-diffusion equation of Li^+ in paper [41]. The total current density for electrons and holes that consists of drift current density and diffusion current density is as shown below:

$$J_n = J_n(drift) + J_n(diffusion) \quad (22)$$

$$J_p = J_p(drift) + J_p(diffusion) \quad (23)$$

where J_n represents the current density for electrons, while J_p represents the current density for holes [42]. The meaning of drift in charge carriers has been described as the movement of the ions caused by an electric field. When an electric field is present in the semiconductor, the electrons are accelerated in the opposite direction of the electric field that is applied and the drift current is generated in the same direction as the electric field. Figure-10 shows the direction of the applied electric field, the direction of drift current, and the direction of charge carriers' movement in semiconductors [43].

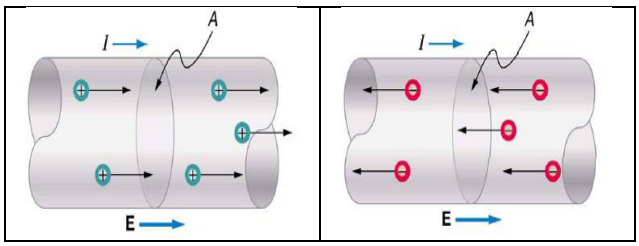

Figure-10. The direction of the applied electric field, the direction of drift current, and the direction of charge carriers' movement in semiconductors [43].

Hence, the electron drift current density can be written as shown in eqn. (25) by using the electron mobility formula as shown in eqn. (24):

$$\mu_n = \frac{1}{2}\frac{qt}{m} \quad (24)$$

$$J_n(drift) = nq\mu_n E \quad (25)$$

where μ_n is electron mobility, t is the time between collisions, q is the magnitude of the electric charge and m is mass of the electron [42]. The hole drift current density can also be derived using the same equations but replacing n with p as shown in eqn. (26) and in eqn. (27):

$$\mu_p = \frac{1}{2}\frac{qt}{m} \quad (26)$$

$$J_P(drift) = pq\mu_P E \quad (27)$$

where p is the hole charge density and μ_p is the hole mobility. Diffusion of the charge carriers in semiconductors is just like diffusion of air in a room. When there is a concentration gradient of the charge carriers, the charge carriers will flow from a high concentration to low concentration until reach equilibrium just like the molecules in the air [42]. In the charge carriers' diffuse process, the diffusion current is generated. The electron diffusion current, $J_n(diffusion)$ will move in the opposite direction from the electron's diffusion, which means from the region with low concentration of electrons to the high concentration. Meanwhile, the hole diffusion current, $J_p(diffusion)$ moves in the same direction of the hole's diffusion, meaning from the high concentration region to the low concentration. Figure-11 shows the concentration of charge carriers with the charge carriers' diffusion direction and the charge carrier diffusion currents directions [44].

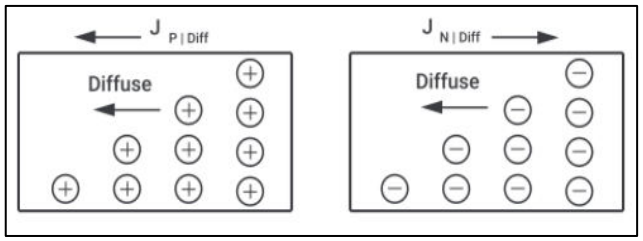

Figure-11. The direction of the applied electric field, the direction of drift current, and the direction of charge carriers' movement in semiconductors [43].

The diffusion current equation for electrons and holes is shown in eqn. (28) and eqn. (29) respectively:

$$J_n(diffusion) = qD_n\frac{\partial n}{\partial x} \quad (28)$$

$$J_p(diffusion) = -qD_p\frac{\partial p}{\partial x} \quad (29)$$

where D_n and D_p are the electrons diffusion coefficient and holes diffusion coefficient respectively [45]. The carrier's diffusion coefficient equations that satisfy the Einstein relationship are shown eqn. (30) and eqn. (31) [46]:

$$D_n = \frac{\mu_n k_b T}{q} \tag{30}$$

$$D_p = \frac{\mu_p k_b T}{q} \tag{31}$$

where k_b is the Boltzmann's constant and T is the temperature in Kelvin. By substituting eqn. (25) and eqn. (28) into eqn. (22), and substituting eqn. (27) and eqn. (29) into eqn. (23), the electron total current density and hole total current density equations are shown in eqn. (32) and in eqn. (33):

$$J_n = nq\mu_n E + qD_n \frac{\partial n}{\partial x} = qD_n \left[\frac{\partial n}{\partial x} - \frac{qn}{k_b T}\left(\frac{\partial \varphi}{\partial x}\right)\right] \tag{32}$$

$$J_p = pq\mu_p E - qD_p \frac{\partial p}{\partial x} = -qD_p \left[\frac{\partial p}{\partial x} + \frac{qp}{k_b T}\left(\frac{\partial \varphi}{\partial x}\right)\right] \tag{33}$$

where $\frac{\partial n}{\partial x}$ and $\frac{\partial p}{\partial x}$ are the electron and hole concentration gradient, while $\frac{\partial \varphi}{\partial x}$ is the electrostatic potential gradient [47].

On the other hand, the continuity equations that express the charge conservation needs to be maintained [45] [48]. The continuity equations consist of current density, generation rate, and recombination rate to describe the variations of charge carriers [49]. The continuity equations can be written below:

$$\frac{\partial n}{\partial t} - \frac{1}{q}\left(\frac{\partial J_n}{\partial x}\right) = G_n(x) - R_n(x) \tag{34}$$

$$\frac{\partial p}{\partial t} + \frac{1}{q}\left(\frac{\partial J_p}{\partial x}\right) = G_P(x) - R_P(x) \tag{35}$$

where $G_n(x)$ and $G_P(x)$ are the generation rates for electrons and holes, while $R_n(x)$ and $R_P(x)$ are the recombination rates for electrons and holes respectively [37] [45] [48]. By referring to Figure-3, eqn. (34) and eqn. (35) expresses the charge conservation at the perovskite layer. For the ETL and HTL layers shown in Figure-3, the $G_n(x)$, $G_P(x)$, $R_n(x)$ and $R_P(x)$ in eqn. (34) and eqn. (35) are equal to zero because there are no generation and recombination of charge carriers occurring at the ETL and HTL.

Generation and Recombination

The generation process of charge carriers in PSC occurs when the photon energy is absorbed by the perovskite material [50]. When the photon energy is larger or equal to the bandgap energy, the electron will gain enough energy and jump from the valence band to the conduction band, while the hole will be left at the valence band after the excitation of the electron. Thus, the free electron and hole pair is generated in the generation process, the electron-hole pair will undergo a drift and diffusion process to generate the current density to conduct current through the external circuit connected between the anode and cathode of PSC [51]. However, the excited electron would not stay at the conduction band forever and it will fall back to the lower energy state in the valence band due to giving up energy to photons, other electrons, or phonons. This reverse process is called recombination [52].

Recombination can be classified as radiative and non-radiative [53]. Radiative recombination occurs when the energy is emitted in the form of photon during the electron falls back from conduction band to the valence band [54]. Meanwhile, non-radiative recombination is defined as the energy that is passed to phonons or released in the form of kinetic energy to another electron during the recombination process [55]. Figure-12 shows the charge carriers recombination mechanisms.

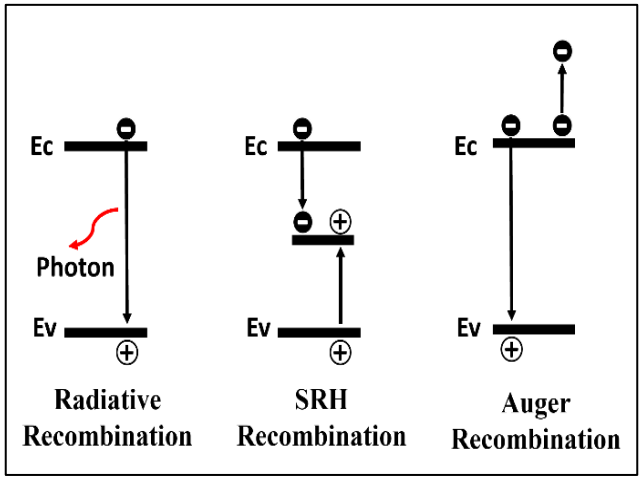

Figure-12. Charge carriers' recombination mechanisms.

Normally, radiative recombination is also called band-to-band recombination. Band-to-band recombination occurs when the electron in the conduction band falls to the valence band that is occupied with holes [55]. Both charge carriers will be neutralized after the band-to-band recombination process and the energy will be released in photon form. The band-to-band recombination is dependent on the density of available electrons and holes. Both carriers must be available during the recombination process [56]. The net recombination rate of band-to-band recombination is proportional to the product of both charge carriers' density, the net recombination rate of band-to-band recombination can be expressed in the equation below:

$$U_{b-b} = b(np - {n_i}^2) \tag{36}$$

where U_{b-b} is the net recombination rate of the band-to-band recombination, where b is the bimolecular recombination constant, and n_i is the intrinsic carrier density [46].

However, when the electron falls from the conduction band to the valence band, it might fall into a 'trap'. The 'trap' refers to an energy level that occurs within the conduction band and valence band which caused by the presence of foreign atom or defect of structure. When the electron falls into the 'trap', the hole at valence band will meet the electron at the 'trap' energy level or the electron that occupying in the trap will further fall to the valance band to meet the hole to complete the recombination process and release energy in the form of photon or multiple phonons [46]. This trap-assist recombination process is one of the non-radiative recombination processes called the Shockley-Read-Hall (SRH) recombination [57]. The SRH recombination involves four steps, which are electron capture, electron emission, hole capture, and hole emission. The eqn. (37) to eqn. (39) shown the expression for SRH recombination:

$$U_{SRH} = \frac{np - {n_i}^2}{\tau_n[p + p_1] + \tau_p[n + n_1]} \quad (37)$$

$$n_1 = n_i exp\left(\frac{E_t - E_i}{k_b T}\right) \quad (38)$$

$$p_1 = n_i exp\left(\frac{E_i - E_t}{k_b T}\right) \quad (39)$$

where U_{SRH} is the net recombination rate of SRH recombination, τ_n and τ_p are the electron and hole minority carrier lifetimes, while E_i and E_t are the intrinsic level and trap state level respectively [48].

Another non-radiative recombination is called the Auger recombination. Auger recombination is similar to band-to-band recombination. The only difference is that the energy released during the transition of electron is transmitted to another electron or hole [58]. As a result, the net recombination rate of Auger recombination is comparable to band-to-band recombination, but the eqn. (40) also considers the density of the electron or hole that absorbs the energy.

$$U_{Auger} = \gamma_n n(np - {n_i}^2) + \gamma_p p(np - {n_i}^2) \quad (40)$$

where U_{Auger} is the net recombination rate of Auger recombination, while γ_n and γ_p are the Auger recombination constant for the electron and hole. The two terms in this equation correspond to the two possible mechanisms [46].

However, because perovskite is a direct bandgap material, the non-radiative recombination is primarily attributed to defects and traps associated with SRH recombination. Auger recombination is insignificant in PSC because of its weaker effect among the non-radiative recombination processes in PSC and because it is not the dominant non-radiative recombination loss when compared to SRH recombination. Therefore, the influence of Auger recombination on PSC performance can be neglected [37][59].

The Steady-State Solutions to the Drift-Diffusion Model

In steady-state, $\frac{\partial n}{dt}$ and $\frac{\partial p}{dt}$ in eqn. (34) and eqn. (35) are assumed to be equal to zero. Because the radiation is removed after steady-state is reached at *t*=0, the excess carrier density returns to zero exponentially with time [60]. According to J.M. Foster *et al* [20]., the current at both contacts of perovskite solar cells (PSC) must be identical and equal to the current flowing at the external circuit during the steady-state condition. Only the steady-state situation is considered and the overall current through the entire device is constant in order to derive the formula for the current-voltage relation of the cell. This can be proved by integrating the hole and electron conservation equations (eqn. (34) and eqn. (35)) in the donor and acceptor that account for the bulk recombination and thermal generation of electron-hole pairs. Besides this, the constant total current throughout the device can also be seen by imposing the continuity of electric current across the interfaces and electron-hole interface. J. M. Foster et al. obtained the dimensionless steady-state problem by rescaling to the steady-state version of the model. This process is similar with the nondimensionalisation of the Doyle-Fuller-Newman (DFN) model in paper [61]. Next, the steady-state problem is solved by J. M. Foster *et al.* with using the software Chebfun and compared the results to the asymptotic solution via predicted current-voltage curves, as well as the potential and charge carrier density profiles [20].

Furthermore, X.Sun *et al*. created a physics-based analytical model to explain the functioning of various perovskite solar cell designs while explicitly considering no uniform generation, carrier selective transport layers, and voltage-dependent carrier collecting [62]. The steady-state electron and hole continuity equations inside the absorber as shown below could be solved to create the analytical model:

$$D_n \frac{\partial^2 n(x)}{\partial x^2} + \mu_n E(x) \frac{\partial n(x)}{\partial x} + G_n(x) - R_n(x) = 0 \quad (41)$$

$$D_p \frac{\partial^2 p(x)}{\partial x^2} - \mu_p E(x) \frac{\partial p(x)}{\partial x} + G_p(x) - R_p(x) = 0 \quad (42)$$

where eqn. (41) and eqn. (42) can be solved analytically to derive the complete current-voltage characteristics of PSC as shown in the equations below:

$$J_{dark} = \left(\alpha_f \times J_{f0} \times \alpha_b \times J_{b0}\right)\left(e^{\frac{qV}{kT}} - 1\right) \quad (43)$$

$$J_{photo} = qG_{max}\left(A - Be^{-\frac{t_o}{\lambda_{ave}}}\right) \quad (44)$$

$$J_{\text{light}} = J_{\text{dark}} + J_{\text{photo}} \quad (45)$$

where α_f, α_b, A, B, and m are the model parameters, J_{f0} and J_{b0} are the dark diode current recombining at the front and back transport layer respectively, in the order of 10^{-13} - 10^{-15} mA/cm^2. G_{max} is the maximum generation of PSC

and can be obtained by integrating the position-dependent photon absorption which is calculated by the transfer matrix method (qG_{max} = 23 mA/cm^2). The model parameters can be expressed using the equations below:

$$\frac{1}{\alpha_f} = \frac{e^{\frac{q(V-V_{bi})}{k_bT}} - 1}{\frac{q(V-V_{bi})}{k_bT}} + \frac{D}{t_o \times s_f} \quad (46)$$

$$\frac{1}{\alpha_b} = \frac{e^{\frac{q(V-V_{bi})}{k_bT}} - 1}{\frac{q(V-V_{bi})}{k_bT}} + \frac{D}{t_o \times s_b} \quad (47)$$

$$A = \alpha_f \times \left\{ \frac{\left(1 - e^{\frac{q(V-V_{bi})}{k_bT} - \frac{t_o}{\lambda_{ave}}}\right)}{\frac{q(V-V_{bi})}{k_bT} - \frac{t_o}{\lambda_{ave}}} - \frac{D}{t_o \times s_f} \right\} \quad (48)$$

$$B = \alpha_b \times \left\{ \frac{\left(1 - e^{\frac{q(V-V_{bi})}{k_bT} + \frac{t_o}{\lambda_{ave}}}\right)}{\frac{q(V-V_{bi})}{k_bT} + \frac{t_o}{\lambda_{ave}}} - \frac{D}{t_o \times s_b} \right\} \quad (49)$$

where t_o is the thickness of the absorber layer (around 300 - 500 nm), λ_{ave} is the average wavelength of the solar spectrum (around 100nm) and D is the diffusion coefficient, which is approximately 0.05 cm^{2}s^{-1}. s_f and s_b are the effective surface recombination velocity at the front and back interface respectively, s_f and s_b could be approximately 10^3 and 10^2 cm/s respectively. V_{bi} is the built-in potential across the absorber layer and can be estimated by using the capacitance-voltage characteristics.

In the end, the model parameters of PSC are extracted by using a fitting algorithm which fits the equations to experimental data. Experimentalists could use this model to define important cell-specific characteristics, identify performance bottlenecks, and forecast the performance of perovskite-based solar panels. The physics-based analytical model developed by X.Sun *et al.* was adapted by P. P. Mondal *et al.* [63] to investigate the performances of basic PSC structures (p-i-n and n-i-p). These performances are the variation of dark current, J_{dark} and photocurrent, J_{photo} density with voltage, the variation of short circuit current density, open circuit voltage, and efficiency with absorber thickness, built-in potential, qG_{max}, and recombination velocity at the backside. P. P. Mondal *et al.* claim that the light current, J_{light} relies on the intensity of the illumination to determine the whole performance, whereas the dark current is illumination independent. In addition, P.P.Mondal *et al.* found that the performance of PSC is significantly influenced by its thickness. The optimal thickness for p-i-n and n-i-p PSC was determined to be 450 nm and 310 nm respectively when all the crucial factors were considered.

THE NUMERICAL SIMULATION OF PSC ANALYTICAL AND DRIFT-DIFFUSION MODEL

Numerical simulation is a form of calculation that is done using the computer to obtain the numerical solutions for the mathematical model of a physical system. The numerical solutions are for the problems that do not have exact solutions, so these solutions need to be guessed and tested by using the method of trial and error until it fulfils certain criteria for the calculation to stop. Normally, these problems involve complex mathematical model for the behaviour of nonlinear systems which need to be solved using analytical solutions.

Numerical Algorithms

Although the analytical equations of solar cell are obtained by characterising the solar cell into the analytical model of a single-diode design, but these equations still need to be solved using numerical methods to obtain the voltage, current, and power of the solar cell because there are still unsolvable parameters when analytical methods are used. Implicit algorithm (IM) is a new method that can determine the electrical parameters of solar cells with fast convergence and is more capable of establishing the final values [35].

Next, the compact model's parameters are then extracted by X.Sun *et al.* [62] using the fitting algorithm to fit equations to the experimental data. After identifying whether or not the absorber is self-doped, the initial assumptions are approximated, and the range of the physical parameters is constrained. The physical parameters are G_{max}, λ_{ave}, t_o, D, s_f, s_b, V_{bi}, J_{f0} and J_{b0}. Next, the fitting process then use MATLAB's iterative fitting function "lsqcurvefit" to fit the photocurrent based on the initial hypotheses with results that greatly depend on the hypotheses at hand. Since the parameters extracted from photocurrent are fixed, the dark current can be found by using the iterative fitting procedure. The self-consistency and convergence between light and dark characteristics must be checked after obtaining the parameters.

Numerical Simulation Software

Beside numerical algorithms, some advanced numerical simulation computer software can be used to simulate the structures of PSC for study, investigation, and understanding the working mechanism to optimize its performance after determining the parameters that are affected. These numerical simulation computer software are SCAPS, AFORS-HET, COMSOL Multiphysics, MATLAB, etc.

SCAPS

SCAPS is software that can solve the three fundamental equations of semiconductors which are Poisson's equation, continuity equations for holes, and continuity equation for electrons by providing the solution through simulation. The three fundamental equations for semiconductors are in the form of coupled partial

differential equations. The profiles of the specified PSC structures including their energy and steady-state band diagram, carrier transport, generation and recombination, bulk defects, electrostatic potential, electric field distributions, and charge carrier concentration can be determined by numerically solving those using SCAPS. Researchers at Gent University in Belgium created SCAPS, which can simulate up to seven levels. I. T. Bello et al. used it to take advantage of the practical device hybrid PSC with defined parameters [64]. Therefore, SCAPS is suitable to simulate the structures of PSC [65].

S. S. Hussain *et al.* [40] simulated a lead-free hybrid double PSC with the structure of Spiro-MeOTAD/(FA)2BiCuI6/TiO2 using SCAPS after solving the continuity differential equations and Poisson differential equations through numerical differentiation and the Gummel type iteration method. The performance of lead-free hybrid double PSC was compared with the lead-based PSC with the structure layer of Spiro-OMeOTAD/$CH_3NH_3PbI_3$/TiO_2. The performance comparison results with 300nm of absorber thickness is shown in Table-3. The results show that the lead-free hybrid double PSC has the potential to replace the lead-based PSC which has high toxicity and can cause harm to the environment. However, when both devices were simulated under conditions with 200nm absorber thickness, the efficiency of the lead-free hybrid double PSC and lead-based PSC was reduced to 22.40% and 24.98% respectively. These simulations result showed that when the thickness of the absorber layer is increased, the PCE is increased. However, according to the simulation results, the absorber layer for lead-free hybrid double PSC can only be increased up to 600 nm. The PCE of lead-free hybrid double PSC dropped beyond 600nm due to the high recombination rate. Besides this, the results regarding the influence of interface defect density and the influence of carrier mobility in lead-free hybrid double PSC also have been discussed by S.S.Hussain et al. with the simulation results from SCAPS [40].

Table-3. The performance of lead-free hybrid double PSC and lead-based PSC [40].

	Spiro-OMeOTAD /$(FA)_2BiCuI_6$/TiO_2	**Spiro-OMeOTAD /$CH_3NH_3PbI_3$/TiO_2**
Jsc (mA cm^{-2})	32.95	34.96
Voc (V)	0.94	0.94
η (%)	24.98	26.43
FF (%)	80.73	80.39

Besides optimising the thickness of absorber layer, studying the donor density at the absorber layer and the total defect density of PSC [66], SCAPS can also be used to investigate the influence of the doping concentration (NA) of the absorber layer as well as the electron affinities of ETM and HTM on the performance of the PSC. Table-4 is the SCAPS results for the influence of the doping concentration (NA) of the absorber layer on the performance of the PSC presented by Eli *et al.* [67] after simulating the PSC with structure layer of glass substrate/TCO/TiO_2/$CH_3NH_3PbI_3$/Cu_2O/metal back contact.

Table-4. The influence of the doping concentration (NA) of absorber layer on the performance of the PSC [67].

NA of absorber layer	**PCE**
10^{14} cm^{-3}	12.99%
10^{15} cm^{-3}	13.82%
10^{16} cm^{-3}	13.21%
10^{17} cm^{-3}	8.40%

The PCE is maximum when NA is 10^{15} cm^{-3}, indicating that at this value, the charge carriers are transported and collected most efficiently. When NA is increased, the built-in electric field is increased in order to increased and separates the charge carriers, enhancing the performance of PSC. Increasing the NA beyond 10^{15} cm^{-3} will also increase the Auger Recombination rate, resulting in a decrease of PCE. This is because, when the Auger Recombination rate is increased up to a certain level, it will suppress the charge carriers transportation and degrade the performance of PSC. Table-5 is the SCAPS results for the influence of the electron affinities of ETM and HTM on the performance of the PSC presented by Eli *et al.* [67].

Table-5. The influence of the electron affinities of ETM and HTM on the performance of the PSC [67].

Electron affinity of Cu_2O (HTM)	**PCE**
3.1 eV to 3.3 eV	Increased
3.3 eV to 3.7 eV	Decreased
Electron affinity of TiO_2 (ETM)	**PCE**
3.7 eV to 4.3 eV	Decreased

The SCAPS results showed that the optimum electron affinity of TiO_2 and Cu_2O are 3.7eV and 3.3 eV respectively. This is because the suitable electron affinity can reduce the recombination of carriers and the performance of PSC can be optimized. The performance of PSC with varying thickness of TiO_2 (ETM), Cu_2O (HTM), and absorber layer ($CH_3NH_3PbI_3$) was also investigated by Eli et al. using SCAPS [67]. Table-6 show the SCAPS results on the influence of ETM, HTM, and absorber layer thickness on the PSC performance. The degradation of PSC performance when the thickness of TiO_2 is increased comes from the fractional absorption of light, the bulk recombination and the surface recombination at the interface. On the other hand, when the thickness of Cu_2O increases, it suggests higher conductivity of the Cu_2O and partial absorption of the light that increases the PCE. Therefore, the optimum thickness of TiO_2 (ETM) and Cu_2O (HTM) is 0.001 μm and 0.160

μm in respectively. On the other hand, when the absorber layer is too thin, the light absorption is poor, but when the thickness of absorber layer is increased up to a certain level, the collection of photogenerated carriers is decreased due to the charge recombination. Therefore, the optimized thickness of absorber layer is 0.4 μm with a PCE of 12.83%. After optimising the thickness of absorber, ETM, HTM, the electron affinity of ETM and HTM, as well as the doping concentration of absorber, Eli et al had simulated a $CH_3NH_3PbI_3$ based PSC by using SCAPS with the performances of PCE = 20.42%, FF = 82.20, Jsc = 22.26 mA cm^{-2} and Voc = 1.12 V [67].

Table-6. The influence of the thickness of ETM, HTM, and absorber layer on the performance of the PSC [67].

Thickness of Cu_2O (HTM)	**PCE**
0.0010 μm to 0.1600 μm	Increased
Thickness of TiO_2 (ETM)	**PCE**
0.0010 μm to 0.1600 μm	Decreased
Thickness of $CH_3NH_3PbI_3$ (Absorber layer)	**PCE**
0.2 μm to 0.4 μm	Increased
0.4 μm to 0.9 μm	Decreased

AFORS-HET

Besides SCAPS, AFORS-HET is also one of the numerical simulations for semiconductors which can simulate one-dimensional semiconductor structures with appropriate boundary conditions under steady-state conditions and small sinusoidal perturbation [68]. The finite difference methods are used to transform the coupled partial differential equations set into the non-linear algebraic equations set to simulate the one-dimensional semiconductor by using AFORS-HET. N.I.Sarkar and H.R.Ghosh have simulated a p-i-n structure amorphous silicon (a-Si: H) thin-film solar cells by using AFORS-HET under conditions T = 300K, AM 1.5 spectrum with 100 mW/cm^2 illumination source. The purpose of this simulation is to study the influences of donor and acceptor concentration, thickness, bandgap, etc. on the electrical performance of a-Si: H thin-film solar cells. Table-7 show the AFORS-HET simulation results for the optimum thickness of a-Si: H solar cell layers with best efficiency [68].

Table-7. The optimum thickness of a-Si: H solar cell layers with best efficiency [68].

Layer of a-Si: H solar cell	**Optimum thickness**
p-layer	0.5 nm to 2.0 nm
n-layer	0.5 nm to 1.0 nm

According to the results of AFORS-HET simulation, when the thickness of p-layer in a-Si: H solar cell increases, the V_{oc}, J_{sc}, η and FF decreases. The result of i-layer thickness variation on the V_{oc}, J_{sc}, FF, and η are similar to the result of p-layer thickness variation, but when the thickness of i-layer is increased up to 500 nm, there were no significant changes for V_{oc}, J_{sc}, FF, and η. For n-layer thickness of a-Si: H solar cell, V_{oc}, J_{sc}, η and FF also decreased beyond 1 nm. Besides that, the optimum value for bandgap is shown in Table-8 and the optimum value for donor concentration of n-layer and acceptor concentration of p-layer is recorded in Table-9.

Table-8. The optimum bandgap of a-Si: H solar cell layers with best efficiency [68].

Layer of a-Si: H solar cell	**Optimum bandgap**
p-layer	1.9 eV to 2.2 eV
i-layer	1.65 eV to 1.75 eV
n-layer	1.95 eV to 2.05 eV

Table-9. The optimum value for donor concentration of n-layer and acceptor concentration of p-layer in a-Si: H solar cell with best efficiency [68].

	Optimum value
Donor concentration of n-layer	7×10^{19} cm^{-3}
Acceptor concentration of p-layer	8.1×10^{19} cm^{-3}

The basic parameter value ranges of AFORS-HET are drawn from established references and all default values have been adopted. The parameters are maintained at their optimal values while a different parameter is changed to determine the highest performing cell structure. After determining the optimum the parameters, the best performances of a-Si:H solar cell were recorded as J_{sc} = −19.87 mA/cm^2, V_{oc} = −0.967 V, FF = 0.689, and Efficiency = 13.26 % [68].

COMSOL Multiphysics

COMSOL Multiphysics is an additional simulation tool that has been extensively utilised in numerical simulation to evaluate different semiconductor devices such as perovskite solar cells. N.K.Elangovan and A.Sivaprakasam [69] has simulated a methylammonium lead iodide ($MAPbI_3$) PSC with device structure of TiO_2/$CH_3NH_3PbI_3$/Spiro-OMeTAD by using one-dimensional (1-D) COMSOL Multiphysics. The optoelectronic modelling of $MAPbI_3$ PSC was performed by linking both electrical and optical responses. Finite element method was used and implemented in COMSOL Multiphysics to optimize the performance of $MAPbI_3$ PSC by varying the thickness of perovskite layer and ETL. The influence of change in the hole blocking layer was analysed using the frequency domain. In the frequency domain, the exact electromagnetic characteristics were calculated by employing 2-D Maxwell's equation in COMSOL Multiphysics. Also, the effect of perovskite layer thickness on the performance of PSC was analysed using stationary solver studies. In the simulation, different thicknesses of perovskite layer in the range of 100-500nm was simulated with a 70nm of ETL thickness, and then the

V_{oc}, J_{sc}, FF, and PCE were recorded. The same simulation was repeated by replacing the ETL thickness with 80nm, 90nm, 100nm, and 110nm, with each of the simulation results recorded and tabulated for further analysis. Table-10 shows the simulation with the highest PCE.

Table-10. The optimum thickness of perovskite layer and ETL of PSC with highest PCE [69].

Highest PCE	17.95%
Optimum thickness of perovskite layer	100nm
Optimum thickness of ETL	90nm

The simulation results also show that when the thickness of ETL was increased beyond 90nm, the PCE decreased. This is because the thicker the ETL, the weaker the light absorption received by the absorber layer to generate electron-hole pair. The simulation results also show that when the thickness of perovskite increased, the performance of the PSC decreased. This is because the thicker the perovskite layer, the higher the series resistance caused by the recombination effect, due to the trapped density and ionic density being large at the interface of ETL and perovskite layer. The recombination effect reduces the generation of photocurrent and efficiency of PSC.

COMSOL Multiphysics is not only outstanding in 1-D simulation, but it is also convenient in two-dimensional (2-D) simulation. F.Jahantigh and S.M.Bagher Ghorashi [70] have compared the performances of well-known $MAPbI_3$ PSC (Cell 1) and the newly developed $Cs_{0.1}FA_{0.74}MA_{0.13}PbI_{2.48}Br_{0.39}$ PSC (Cell 2) with two HTM layers using a two-dimensional (2-D) modular model that was developed in COMSOL Multiphysics to study the influences of HTM, the optimum thickness of each layer and the overall thickness of PSC. Table-11 and Table-12 shows the optimum thickness of layers for Cell 1 and Cell 2 obtained from the results of the simulation respectively.

Table-11. The optimum thickness of layers for cell 1 [70].

Layer of PSC	Optimum thickness
HTM (Spiro-OMeTAD)	110 nm
ETM (TiO_2)	30 nm
Perovskite ($MAPbI_3$)	390 nm
Total Thickness	530 nm

Table-12. The optimum thickness of layers for cell 2 [70].

Layer of PSC	Optimum thickness
HTM (Spiro-OMeTAD)	130 nm
HTM (TTA3)	20 nm
ETM (TiO_2)	35 nm
Perovskite ($MAPbI_3$)	410 nm
Total Thickness	595 nm

F. Jahantigh and S. M. Bagher Ghorashi found that, when the thickness of Spiro-OMeTAD increases, so does the PCE. However, the thickness of Spiro-OMeTAD was not the only factor that will affect the PCE. Lower optimum thickness of Spiro-OMeTAD might be obtained by combining it with other layers contained in PSC. According to the simulation results, when the total thickness of HTM layer in Cell 2 was higher than in Cell 1, the PCE of Cell 2 was also higher than Cell 1 which was recorded as 26.1% and 20.7% respectively [70].

Besides two-dimensional (2-D) analysis, COMSOL Multiphysics packages that include the wave optics module, semiconductor module, and heat transfer in solid module can also perform the simulation in three-dimensional (3-D) configurations. P.Saxena and N.E.Gorji [71] have investigated the temperature distribution in the conventional perovskite solar cells via a numerically solved couple optical-electrical–thermal (OET) modules by using COMSOL platform in 3-D scheme. This is due to the fact that the performance of solar cells is significantly impacted by heat dissipation, but this phenomenon is not fully investigated. Furthermore, COMSOL may be used to do thermal analyses of various device topologies, including perovskite solar cells and other thin-film devices, in addition to calculating the charge carrier production profile. The COMSOL heat transfer module can simulate the thermal processes that occur in electrical components and offers a great setting for looking at how heat is distributed in PSCs that are really running in the real world. The simulation results of COMSOL show the electron and hole concentration profile, electric field profile, heat distribution profile, temperature distribution under operation profile, SRH recombination profile, temperature gradient magnitude profile, and total heat flux magnitude profile. Table-13 shows the simulation results of electron and hole concentration profile [71].

Table-13. The simulation results of electron and hole concentration profile [71].

Layer of PSC	HTM (Spiro-OMeTAD)	ETM (TiO_2)
Concentration of Hole	Lowest	Highest
Concentration of Electron	Highest	Lowest

According to the electric field profile, the electric field is intensive at the TiO_2/perovskite and Spiro-OMeTAD/Au. The SRH recombination shows the maximum value within the perovskite layer as shown in SRH recombination profile, while the higher the SRH recombination, the higher the heat generated within the perovskite layer. Another heat that is produced by current conduction is called the Joule heat. The highest Joule heat shown in the heat distribution profile was recorded within the layer of TiO_2/perovskite, because the electric field was also intensive at this layer. Next, there is almost no temperature difference across the cell when the cell has just reached a stationary operation mode as shown in temperature distribution under the operation profile. This

is most probably due to the whole PSC is relatively thin. We can see from the overall heat flux magnitude profile that the performance and stability of PSC depend heavily on the heat dissipation at the electrode. In order to promote stability against the rising temperature under normal operating conditions, the metallic contact of PSC must be chosen as a highly heat conductive material to speed up the heat dissipation on the bottom of PSC. A flaw in PbI_2 caused by the oxidation or disintegration of the perovskite layer following exposure to moisture may weaken the stability of PSC in addition to the temperature analysis. COMSOL simulations can also be used to explore the moisture effect and ion electro migration in the perovskite layer, which may not be viable using the one-dimensional (1-D) simulation platforms that are currently accessible. TCAD simulation is another 3-D simulation platform in addition to COMSOL that is frequently used for optical or electrical simulations of semiconductor devices using the finite element method or finite-difference time-domain approaches.

MATLAB

Besides finite difference methods (FDMs) used in AFORS-HET [68] and finite element methods (FEMs) used in COMSOL Multiphysics [70], in order to solve the models of charge carrier movement and ion vacancy migration in perovskite solar cells, MATLAB's ode15s may evolve ordinary differential-algebraic equations (ODEs) using time as the independent variable that are reduced from partial differential equations (PDEs) [21]. In comparison to the finite difference scheme and certain formerly employed alternative approaches in MATLAB such as CHEBFUN and PDEPE, the finite element scheme offers noticeably higher accuracy and faster processing time, claim N. E. Courtier et al [21]. For instance, the finite element approach can compute the transient sweep of a current-voltage curve for realistic parameter values in just a few seconds on a typical desktop computer, using about 50 times as less computational work as the other methods mentioned so far [21]. Therefore, a realistic charge transport model for a metal halide PSC may be numerically solved using the finite difference scheme.

CONCLUSIONS

In a nutshell, third-generation solar cells have reduced the drawback of previous-generation solar cells which is the high manufacturing cost of first-generation solar cells as well as the toxicity and material rarity of second-generation solar cells. Many factors could affect the performance of PSC. These factors include the structure architectures, the materials, and thickness of each layer, the generation, recombination, drift and diffusion of charge carriers, defect density, and so on. Through the modelling process, the factors that affect the performances of PSC can be determined and can be further studied to optimize the parameters to enhance the performances of PSC. In this review paper, circuitry modelling and electrochemical modelling are discussed with analytical solutions and numerical simulation. In circuitry modelling, the PSC structure is represented in the equivalent circuit model while in electrochemical modelling, the drift-diffusion model of the PSC is presented in mathematical equations form. The equivalent circuit model can be designed depending on the complexity of PSC structure and the accuracy of simulation results that are wished to be obtained. Electrical equations can be obtained from the designed equivalent circuit model and solved using mathematical functions such as Lambert W-function or Implicit algorithm (IM) to determine the electrical parameters of solar cells. Besides numerical algorithms, some advanced numerical simulation software is used, for example, SCAPS, AFORS-HET, COMSOL Multiphysics, MATLAB, etc. This numerical simulation software is used to simulate the PSC for different purposes, for example comparing the performances of different types of PSC, enhancing the PSC performance by optimising the layer thickness of ETL, HTL, and absorber, studying the impact of total defect density on the PSC efficiency, investigate the influence of the doping concentration (NA) of the absorber layer and the electron affinities of ETM and HTM on the PSC performance, as well as investigated the temperature distribution in the PSC.

ACKNOWLEDGEMENT

This work is supported by Universiti Teknikal Malaysia Melaka (UTeM) and is funded by the Ministry of Higher Education Malaysia under the Fundamental Research Grant Scheme (FRGS): FRGS/1/2020/STG06/UTEM/02/2. Furthermore, we would like to acknowledge the support from Solar Cell Research Institute UKM (SERI) who provides the valuable inputs for perovskite cell.

REFERENCES

[1] N. Kannan and D. Vakeesan. 2016. Solar energy for future world : - A review. 62: 1092–1105, doi: 10.1016/j.rser.2016.05.022.

[2] L. M. Fraas. 2014. History of Solar Cell Development. Low-Cost Sol. Electr. Power, pp. 1–12, doi: 10.1007/978-3-319-07530-3_1.

[3] Roberto Parato Parato, Fill It Up, Please! Lulu Press, Inc, 2020. Accessed: Jan. 11, 2022. [Online]. Available: https://books.google.com/books/about/Fill_It_Up_Please.html?id=BMzKDwAAQBAJ

[4] N. Akter. 2017. Study on Structural, Optical and Electrical Properties of Single Junction Mono-crystalline Silicon Solar Cells. No. 138.

[5] K. S. Ahmad, S. N. Naqvi and S. B. Jaffri. 2021. Systematic review elucidating the generations and classifications of solar cells contributing towards

environmental sustainability integration. Rev. Inorg. Chem., 41(1): 21-39, doi: 10.1515/revic-2020-0009.

[6] I. Hussain, H. P. Tran, J. Jaksik, J. Moore, N. Islam and M. J. Uddin. 2018. Functional materials, device architecture, and flexibility of perovskite solar cell. Emergent Mater. 1(3–4): 133-154, doi: 10.1007/s42247-018-0013-1.

[7] T. Zhang, M. Wang, and H. Yang. 2018. A review of the energy performance and life-cycle assessment of building-integrated photovoltaic (BIPV) systems. Energies, 11(11), doi: 10.3390/en11113157.

[8] E. Generation. 2019. Engineered Nanomaterials for Energy Applications. pp. 751-767, doi: 10.1016/B978-0-12-813351-4.00043-2.

[9] G. Richhariya, A. Kumar and Samsher. 2020. Solar cell technologies. Elsevier Inc., doi: 10.1016/b978-0-12-819610-6.00002-8.

[10] 2020. Best Research-Cell Efficiency Chart | Photovoltaic Research | NREL. https://www.nrel.gov/pv/cell-efficiency.html (accessed Jan. 12, 2022).

[11] T. D. Lee and A. U. Ebong. 2016. A review of thin fi lm solar cell technologies and challenges. Renew. Sustain. Energy Rev., no. December, pp. 0-1, doi: 10.1016/j.rser.2016.12.028.

[12] K. Sharma, V. Sharma, and S. S. Sharma. 2018. Dye-Sensitized Solar Cells : Fundamentals and Current Status. Vol. 6.

[13] M. A. Mingsukang, M. H. Buraidah, and A. K. Arof. 2017. Third-Generation-Sensitized Solar Cells. Nanostructured Sol. Cells, doi: 10.5772/65290.

[14] A decade of perovskite photovoltaics. 2019. Nat. Energy 2019 41, 4(1): 1-1, doi: 10.1038/s41560-018-0323-9.

[15] M. Kaur and H. Singh. 2016. A Review : Comparison of Silicon Solar Cells and Thin Film Solar Cells. Int. J. Core Eng. Manag. 3(2): 15-23.

[16] S. Ananthakumar, J. R. Kumar and S. M. Babu, Third-Generation Solar Cells: Concept, Materials and Performance - An Overview. 2019. doi: 10.1007/978-3-030-04474-9_7.

[17] A. Bashir and M. Sultan. 2020. Organometal Halide Perovskite-Based Materials and Their Applications in Solar Cell Devices. Solar Cells. Springer Nature Switzerland, pp. 259-281, doi: 10.1007/978-3-030-36354-3_10.

[18] K. P. Bhandari and R. J. Ellingson. An Overview of Hybrid Organic–Inorganic Metal Halide Perovskite Solar Cells. Elsevier Inc., 2018. doi: 10.1016/b978-0-12-811479-7.00011-7.

[19] D. Zhou, T. Zhou, Y. Tian, X. Zhu, and Y. Tu. 2018. Perovskite-Based Solar Cells : Materials, Methods, and Future Perspectives. Vol. 2018.

[20] J. M. Foster, H. J. Snaith, T. Leijtens, and G. Richardson. 2014. A model for the operation of perovskite based hybrid solar cells: Formulation, analysis, and comparison to experiment. SIAM J. Appl. Math., 74(6): 1935-1966, doi: 10.1137/130934258.

[21] N. E. Courtier, G. Richardson and J. M. Foster. 2018. A fast and robust numerical scheme for solving models of charge carrier transport and ion vacancy motion in perovskite solar cells. Appl. Math. Model. 63: 329-348, doi: 10.1016/j.apm.2018.06.051.

[22] P. Mandon and E. Prasad. 2021. Perovskite Solar Cell Market Growth Forecast-2030 | Size, Share. Allied Market Research, https://www.alliedmarketresearch.com/perovskite-solar-cell-market-A13745 (accessed Mar. 26, 2022).

[23] G. Overton. 2013. Perovskite solar cells 5X cheaper than comparable thin-film technology | Laser Focus World. Laser Focus World, https://www.laserfocusworld.com/test-measurement/research/article/16561288/perovskite-solar-cells-5x-cheaper-than-comparable-thinfilm-technology (accessed Mar. 26, 2022).

[24] T. Ouslimane, L. Et-taya, L. Elmaimouni, and A. Benami. 2021. Impact of absorber layer thickness, defect density, and operating temperature on the performance of MAPbI3 solar cells based on ZnO electron transporting material. Heliyon, 7(3): e06379, 2021, doi: 10.1016/j.heliyon.2021.e06379.

[25] T. Xu, Z. S. Wang, X. H. Li and W. E. I. Sha. 2021. Loss mechanism analyses of perovskite solar cells with equivalent circuit model. Wuli Xuebao/Acta Phys. Sin., 70(9): 1-17, doi: 10.7498/aps.70.20201975.

[26] P. Liao, X. Zhao, G. Li, Y. Shen and M. Wang. 2018. A New Method for Fitting Current – Voltage Curves of Planar Heterojunction Perovskite Solar Cells. Nano-Micro Lett., 10(1): 1-8, doi: 10.1007/s40820-017-0159-z.

[27] E. Velilla, J. B. Cano, K. Jimenez, J. Valencia, D. Ramirez, and F. Jaramillo. 2018. Numerical analysis to determine reliable one-diode model parameters for perovskite solar cells. Energies, 11(8), doi: 10.3390/en11081963.

[28] Gagandeep, M. Singh, R. Kumar, V. Singh, and F. Chand. 2018. A theoretical study of perovskite material for solar cell application. AIP Conf. Proc., 2006(August): 4–9, doi: 10.1063/1.5051274.

[29] J. Esteban and V. Delgado. 2017. Characterization of Solar Cells : Dark current measurements.

[30] M. Z. Kabir. 2021. A physics-based analytical model for current-voltage characteristics of perovskite solar cells incorporating bulk recombination. Energies, 14(13), doi: 10.3390/en14133868.

[31] A. Bărar, C. Boscornea, M. Bălăşoiu, and D. Mănănăilă-Maximean. 2021. Two-diode modelling of perovskite solar cells and parameter extraction using the lambert w function. UPB Sci. Bull. Ser. A Appl. Math. Phys. 83(4): 285-294.

[32] V. Khanna, B. K. Das, D. Bisht, Vandana and P. K. Singh. 2015. A three diode model for industrial solar cells and estimation of solar cell parameters using PSO algorithm. Renew. Energy, 78: 105-113, doi: 10.1016/j.renene.2014.12.072.

[33] D. S. Abdelminaam, M. Said and E. H. Houssein. 2021. Turbulent Flow of Water-Based Optimization Using New Objective Function for Parameter Extraction of Six Photovoltaic Models. IEEE Access, 9: 35382-35398, doi: 10.1109/ACCESS.2021.3061529.

[34] N. Santakrus, L. Kumar and V. Kumar. 2021. Solving the equivalent circuit of a planar heterojunction perovskite solar cell using Lambert W-function. Solid State Commun., 337(July): 114439, 2021, doi: 10.1016/j.ssc.2021.114439.

[35] M. Rasheed, O. Alabdali and S. Shihab. 2021. A New Technique for Solar Cell Parameters Estimation of the Single-Diode Model. J. Phys. Conf. Ser., 1879(3): 1-10, doi: 10.1088/1742-6596/1879/3/032120.

[36] W. He, M. Pecht, D. Flynn and F. Dinmohammadi. 2018. A Physics-Based Electrochemical Model for Lithium- Ion Battery State-of-Charge Estimation Solved by an Optimised Projection-Based Method and Moving- Window Filtering. pp. 1-24, doi: 10.3390/en11082120.

[37] X. Ren, Z. Wang, W. E. I. Sha and W. C. H. Choy. 2017. Exploring the Way to Approach the Efficiency Limit of Perovskite Solar Cells by Drift-Diffusion Model. doi: 10.1021/acsphotonics.6b01043.

[38] A. Zangwill, Modern Electrodynamics. 2012. doi: 10.1017/cbo9781139034777.

[39] G. W. Richardson, J. M. Foster, R. Ranom, C. P. Please and A. M. Ramos. 2021. Charge transport modelling of Lithium-ion batteries. Eur. J. Appl. Math., vol. 71, doi: 10.1017/S0956792521000292.

[40] S. S. Hussain *et al.* 2021. Numerical Modeling and Optimization of Lead-Free Hybrid Double Perovskite Solar Cell by Using SCAPS-1D. J. Renew. Energy, vol. 2021, pp. 1–12, 2021, doi: 10.1155/2021/6668687.

[41] R. Ranom and H. N. A. Rosszainily. 2019. Lithium Ion Battery Performance for Different Size of Electrode Particles and Porosity. (1): 4401-4405, doi: 10.35940/ijitee.A5086.119119.

[42] S. Ekhagen. 2017. Silicon solar cells: basics of simulation and modelling Using the mathematical program Maple to simulate and model a silicon solar cell Kisel solceller: Grunderna för simulering och modellering.

[43] 2016. Douglas College Physics 1104: Fall 2019 and winter 2020. [Online]. Available: pressbooks.bccampus.ca/introductorygeneralphysics1phys1107

[44] Susie Maestre. 2020. What is the difference between drift and diffusion… | CircuitBread. May 22, https://www.circuitbread.com/ee-faq/what-is-the-difference-between-drift-and-diffusion-currents-in-a-semiconductor (accessed Jan. 27, 2022).

[45] D. Li, L. Song, Y. Chen and W. Huang. 2020. Modeling Thin Film Solar Cells : From Organic to Perovskite. vol. 1901397, doi: 10.1002/advs.201901397.

[46] V. Zeghbroeck. 2004. Principles of Semiconductor Devices.

[47] N. A. A. Rahim, R. Ranom, and H. Zainuddin. 2018. Mathematical Modelling of Surface Discharge on the Contaminated Surface of Insulator Using Nernst's Planck Equation. 10(2): 5-10.

[48] Y. Huang. 2018. Drift diffusion modelling of perovskite based solar cells, III-V optoelectronic devices and Kelvin probe force microscopy.

[49] M. Kunrugsa and A. S. C. Structure. 2019. Theoretical Study of Multi-stacked GaSb / GaAs Quantum Dot Solar Cells. pp. 13-16.

[50] S. Nazerdeylami. 2020. Dominant recombination mechanism in perovskite solar cells: A theoretical study. Sol. Energy, 206(May): 27-34, doi: 10.1016/j.solener.2020.05.095.

[51] J. Shi *et al.* 2018. From Ultrafast to Ultraslow: Charge-Carrier Dynamics of Perovskite Solar Cells. Joule, 2(5): 879-901, doi: 10.1016/j.joule.2018.04.010.

[52] B. Theories and S. Electrochemistry. 2005. Basic Theories of Semiconductor Electrochemistry. Electrochem. Silicon Its Oxide, pp. 1-43, doi: 10.1007/0-306-47921-4_1.

[53] D. W. Dequilettes *et al.* 2019. Charge-Carrier Recombination in Halide Perovskites. Chem. Rev., 119(20): 11007-11019, doi: 10.1021/acs.chemrev.9b00169.

[54] G. P. Agrawal and N. K. Dutta. 1993. Recombination Mechanisms in Semiconductors. Long-Wavelength Semicond. Lasers, pp. 70-141, 1993, doi: 10.1007/978-94-011-6994-3_3.

[55] K. W. Böer and U. W. Pohl, Carrier Recombination and Noise. 2020. doi: 10.1007/978-3-319-06540-3.

[56] M. L. Inche Ibrahim and A. A. Zakhidov. 2022. An improved model for describing the net carrier recombination rate in semiconductor devices. Appl. Phys. A Mater. Sci. Process., 128(1): 1-26, doi: 10.1007/s00339-021-05104-5.

[57] S. Zeiske, O. J. Sandberg, N. Zarrabi, W. Li, P. Meredith and A. Armin. 2021. Direct observation of trap-assisted recombination in organic photovoltaic devices. Nat. Commun., 12(1): 1-7, doi: 10.1038/s41467-021-23870-x.

[58] M. B. Johnston and L. M. Herz. 2016. Hybrid Perovskites for Photovoltaics: Charge-Carrier Recombination, Diffusion, and Radiative Efficiencies. Acc. Chem. Res., 49(1): 146-154, doi: 10.1021/acs.accounts.5b00411.

[59] J. Chen and N. G. Park. 2019. Causes and Solutions of Recombination in Perovskite Solar Cells. Adv. Mater., 31(47): 1-56, doi: 10.1002/adma.201803019.

[60] O. Ragb. 2021. An accurate numerical approach for studying perovskite solar cells. (May): 1-22, doi: 10.1002/er.6892.

[61] G. Richardson, I. Korotkin, R. Ranom, M. Castle and J. M. Foster. 2020. Generalised single particle models for high-rate operation of graded lithium-ion electrodes: Systematic derivation and validation. Electrochim. Acta, 339: 135862, doi: 10.1016/j.electacta.2020.135862.

[62] X. Sun, S. Member, R. Asadpour, W. Nie, A. D. Mohite and M. A. Alam. 2015. A Physics-Based Analytical Model for Perovskite Solar Cells. 5(5): 1389-1394.

[63] P. P. Mondal, M. S. H. Khan, M. R. Kaysir and M. R. Islam. 2019. Performance Analysis of Perovskite Solar Cells with Different Structures. no. February, 2019, doi: 10.1109/ECACE.2019.8679329.

[64] I. T. Bello, Y. A. Odedunmoye, O. Adedokun, H. A. Shittu and A. O. Awodugba. 2019. Numerical simulation of sandwiched Perovskite-based solar cell using solar cell capacitance simulator (SCAPS-1D). J. Niger. Soc. Phys. Sci., 1(2): 57-61, doi: 10.46481/jnsps.2019.11.

[65] A. C. Nkele, I. S. Ike, S. Ezugwu, M. Maaza and F. I. Ezema. 2021. An overview of the mathematical modelling of perovskite solar cells towards achieving highly efficient perovskite devices. Int. J. Energy Res., 45(2): 1496-1516, doi: 10.1002/er.5987.

[66] D. Sharma. 2022. Mathematical Modelling and Simulation of CH3NH3Pb (I1-Xbrx) 3 Based Perovskite Solar Cells For High E ciency.

[67] D. Eli *et al.* 2019. Simulation and optimization of lead-based perovskite solar cells with cuprous oxide as a P-type inorganic layer. J. Niger. Soc. Phys. Sci., 1(2): 72-81, doi: 10.46481/jnsps.2019.13.

[68] N. I. Sarkar and H. R. Ghosh. 2017. Efficiency improvement of amorphous silicon single junction solar cell by design optimization. ECCE 2017 - Int. Conf. Electr. Comput. Commun. Eng., pp. 670-675, doi: 10.1109/ECACE.2017.7912989.

[69] N. K. Elangovan and A. Sivaprakasam. 2021. Investigation of parameters affecting the performance of Perovskite solar cells. Mol. Cryst. Liq. Cryst., 710(1): 66-73, doi: 10.1080/15421406.2020.1829425.

[70] F. Jahantigh and S. M. Bagher Ghorashi. 2019. Optical Simulation and Investigation of the Effect of Hysteresis on the Perovskite Solar Cells. doi: 10.1142/S1793292019501273.

[71] P. Saxena and N. E. Gorji. 2019. COMSOL Simulation of Heat Distribution in Perovskite Solar Cells: Coupled Optical-Electrical-Thermal 3-D Analysis. IEEE J. Photovoltaics, 9(6): 1693-1698, doi: 10.1109/JPHOTOV.2019.2940886.